Measurement of the H($n=2$) density matrix for 20–100-keV collisions of H^+ on He

Robert Cline,* P. J. M. van der Burgt,† W. B. Westerveld,‡ and J. S. Risley
Atomic Collisions Laboratory, Department of Physics, North Carolina State University, Raleigh, North Carolina 27695-8202
(Received 1 March 1993; revised manuscript received 9 November 1993)

Density matrices are experimentally determined which describe H($n=2$) atoms produced in electron-transfer collisions between 20–100-keV protons and helium. The density matrix contains the electron-transfer cross sections σ_{2s}, σ_{2p_0}, and $\sigma_{2p_{\pm 1}}$, as well as the real and imaginary parts of the s_0p_0 coherence. Experimentally, a monoenergetic proton beam traverses a helium gas cell producing hydrogen atoms H(n) via electron transfer. Within the gas cell an electric field is applied either axial or transverse to the proton beam. The Stokes parameters describing the intensity and linear polarization of Lyman-α radiation (122 nm) emitted by H($n=2$) atoms are determined as a function of applied electric-field strength. The density-matrix elements are determined from a linear least-squares fit of the Stokes parameters to the set of five fitting functions which represent the contributions from individual density-matrix elements. The density-matrix results are self-consistent. Separate determinations using axial or transverse electric fields agree with each other. The general results indicate $\sigma_{2s} > \sigma_{2p_0} > \sigma_{2p_{\pm 1}}$ between 20 and 100 keV. The electric dipole moment $\langle \mathbf{d} \rangle_z$ has a value near zero at 20 keV rising to a maximum of about 1.3 a.u. near 40 keV and remaining nearly constant through 100 keV. The $\langle \mathbf{L} \times \mathbf{A} \rangle_{z,s}$ moment has a maximum of about 0.5 a.u. at 25 keV, passing through zero near 70 keV. These results compare favorably with available experimental results and are qualitatively predicted by present theoretical models. Comparison with previous H($n=3$) results indicates that the Runge-Lenz vector $\langle \mathbf{A} \rangle_z$ is larger for $n=3$ than for $n=2$ and that $\langle \mathbf{L} \times \mathbf{A} \rangle_{z,s}$ has the same values for both n.

PACS number(s): 34.70.+e, 34.50.Fa, 32.60.+i, 07.60.Fs

I. INTRODUCTION

Collisions probe the interactions of atoms by determining the change in the population of atomic energy levels caused by the collision. Modeling atomic collision processes presents a great challenge because of the large number of channels available in the collision. In an effort to determine the important channels in collisions and in order to further our understanding of the collision process, this laboratory has undertaken a systematic study of fundamental atomic collisions. The research has primarily concentrated on collisions between protons and helium [1–9]. The process where one electron is transferred from the helium atom to the proton, forming a hydrogen atom, is the dominant channel in this collision within the considered energy range. The focus of the experimental research in this laboratory has been the study of electron transfer into excited states of hydrogen.

The electron-transfer process may be written as

$$H^+ + He \rightarrow H(n) + He^+ ,$$

where n is the principal quantum number used to label the eigenstates of hydrogen. Because the scattering angles of the hydrogen atoms are not detected, the most complete description of the collision uses a density matrix [10] to describe the hydrogen atoms at the time of their production. The density matrix contains cross sections for the production of the various angular momentum eigenstates of H(n) as well as coherences between these eigenstates. The cross sections, diagonal density-matrix elements, describe the probability of collisionally populating a particular eigenstate. The coherences, off-diagonal density-matrix elements, are proportional to the phase difference between two eigenstates, implicitly averaged over scattering angles in the collision. The H($n=3$) density matrix is described by 14 equal non-zero independent parameters while the H($n=2$) density matrix contains only 5. Previous research [8] has determined the density matrices describing H($n=3$) for proton energies of 20–100 keV, while this work details the experimental determination of H($n=2$) density matrices for the same energy range.

Experimental measurements of collisionally produced coherence have been made since 1970. The H($n=2$) system has played an important role in experimental demonstrations of coherence in beam-foil and proton-atom collisions [11–15]. In these other experiments the intensity of Lyman-α radiation (122 nm) emitted from the radiative decay H($n=2 \rightarrow n=1$) is measured as a function of time after the collision. The measured intensity exhibits quantum beats, an oscillation of the intensity due to coherent population of H($n=2$) energy levels with nearly the same energy. These measurements are performed in the presence of an electric field which Stark-mixes the H($n=2$) manifold. Stark mixing is necessary to observe

*Present address: Department of Physics, University of Texas, Austin, TX 78712.
†Present address: Department of Physics, University of Windsor, Windsor, Ontario, Canada N9B 3P4.
‡Permanent address: Department of Physics, University of Utrecht, NL3584 CC Utrecht, The Netherlands.

any radiation due to population of the H(2s) eigenstate since field-free radiative decay from H(2s) is forbidden via an electric dipole transition. The effect of electric fields on hydrogen atoms is a topic of continuing interest in atomic physics [16–18]. Previous work in this laboratory used electric fields with a different experimental method to determine cross sections and coherences. This work uses the same experimental method, which is described below.

In previous research [6] the H($n=3$) density matrix was determined by observation of Balmer-α radiation (656 nm) emitted from the radiative decay H($n=3 \rightarrow n=2$). The atoms decay in an electric field applied axially or transversely to the beam direction. A measurement of the intensity and polarization of the emitted light is analyzed to yield density-matrix elements describing the excited atom.

The analysis of the experimental data is a statistical fit to a set of fitting functions which represent the contributions to the experimental signal from individual density-matrix elements. The fitting functions are numerically calculated on a supercomputer using a sophisticated analysis which accounts for the time evolution of hydrogen atoms in an electric field from the time of their formation until the time of their radiative decay. This analysis includes the effects of cascade, optical detection efficiency, and inhomogeneities in helium gas density and electric-field strength. Considerable effort has been made to ensure that all possible systematic effects are accounted for in this analysis.

This experimental strategy is used in this work to determine experimentally density matrices describing H($n=2$) produced in 20–100-keV electron-transfer collisions of protons and helium. The organization of this paper is as follows: The experimental apparatus, with emphasis on the optical system used in the polarization analysis of the Lyman-α radiation, is described in Sec. II. A brief review of the data analysis is given in Sec. III, with an emphasis on the difference between the $n=3$ experiment and the present experiment. Section IV contains the results and their comparison with various theoretical models, other experimental studies of H($n=2$), and previous research on H($n=3$).

II. EXPERIMENTAL APPARATUS

A. General

The apparatus used in these experiments has previously been described [3,6], so only a brief outline will be given here. Protons are accelerated to energies between 20 and 100 keV and sent into the collision region shown in Fig. 1. Either an axial or a transverse electric field is applied in the cell by electrodes which are not shown. Beam currents, measured by a Faraday cup, are usually about $1-2\ \mu$A at the end of the line. He gas (of 99.999% purity) for the collision is fed in at the end of the chamber through a precision leak valve. The entrance aperture of the cell serves to isolate the collision region from the front part of the chamber. Condensable contaminants are removed with a liquid-nitrogen-filled cold finger. The cell pressure is determined absolutely by a capacitance manometer and maintained at 1 to 3 mTorr.

Lyman-α light emitted from excited H atoms in the target cell is observed by the optical detection system shown in Fig. 2. Contributions to the signal from collisions with background gas in front of the target cell are removed by an automated subtraction technique wherein target gas is periodically routed to the region upstream of the cell, and the difference taken between signals measured both with gas in the cell and with gas admitted upstream of the cell. In order to account for pressure changes in the background subtraction and for possible beam drifts, optical signals are normalized to both the beam current, integrated during the measurement time from the Faraday cup, and to the cell pressure, determined from integration of the current from an ion gauge.

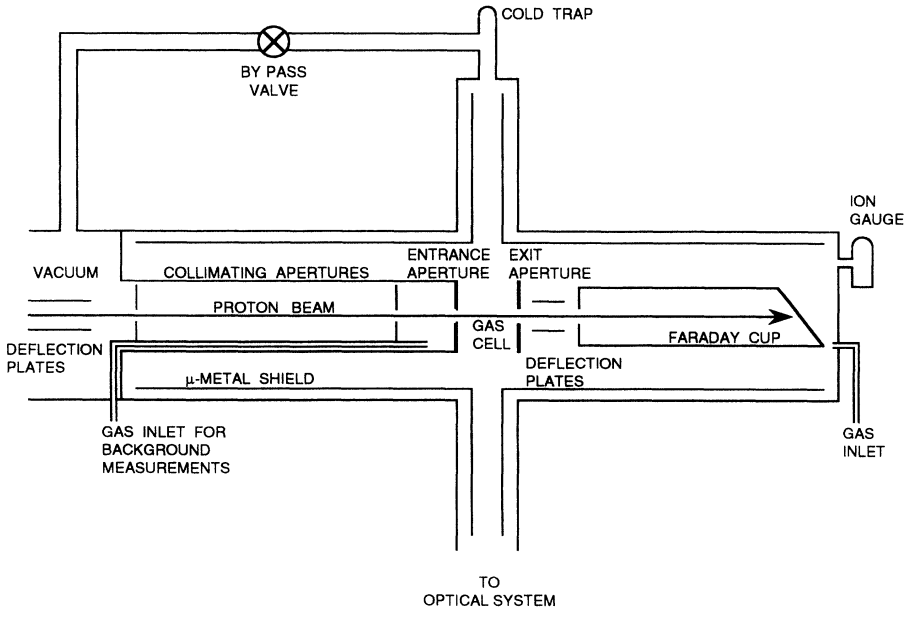

FIG. 1. General overview of experimental apparatus.

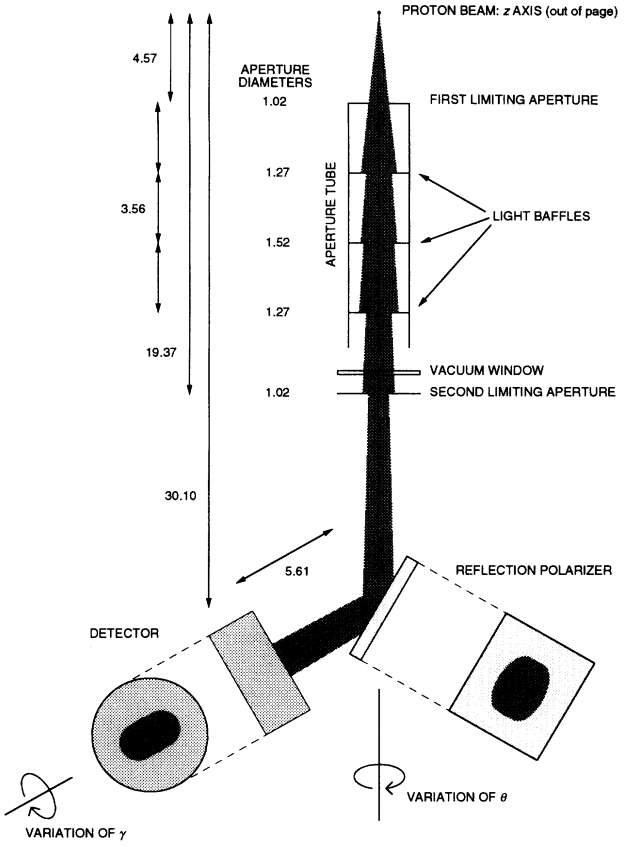

FIG. 2. Overview of the optical system. All dimensions are given in cm.

A correction for the 5–10% beam attenuation occurring with target gas in the cell has been measured with ±10% precision and is included in the data analysis. A correction for the additional proton acceleration provided by the axial electric field was also included. Careful checks of the signal linearity with respect to pressure were compared to computer simulations using known values of experimental cross sections to ensure single-collision conditions in the gas cell.

We measure the intensity and polarization of the Lyman-α light as a function of the electric field applied in the target cell. Electric fields of ±280 V/cm in the axial case and ±400 V/cm in the transverse case are selected from a standard set and applied in random order. As mentioned before, each nonzero-field optical measurement is followed by a zero-field optical measurement for normalization.

Light is emitted in all directions from excited atoms in the beam. Only light that passes through the two limiting apertures reaches the detector. The limiting apertures define the viewing region, the region of the beam which is in view of the detector. Between the two limiting apertures are three light baffles which eliminate reflections from the aperture tube. Just prior to the second limiting aperture is a LiF vacuum window which allows a pressure difference between the optical chamber and the gas cell. The 2-mm-thick window transmits about 50% of the incident Lyman-α radiation, and has a transmission cutoff at a wavelength of 105 nm.

The light is incident on a reflection linear polarizer which consists of a plane mirror made from optical glass SF6 oriented at 60° angle of incidence. Its reflectance is about $R=25\%$ and its polarization is $P=81.2\pm2.4\%$. The azimuthal alignment between the reflection polarizer and the z axis is better than 0.5°. After reflecting from the linear polarizer, the light is incident on an electron multiplier (EM) which multiplies photoelectrons given off by its first dynode, pulses from which are counted. The EM (Hamamatsu Model R2363) is insensitive to light with a wavelength greater than about 160 nm.

In order to analyze the experimental measurements, we need to know the exact location of the viewing region with respect to the entrance plate of the gas cell. In other words, we need to know the solid angle subtended by the optical system as a function of position along the proton beam. In Fig. 2 the shaded area indicates the region illuminated by the entire viewing region. The sold lines on the fold-out views of the mirror and detector indicate the region illuminated by the central point of the viewing region.

The technique to experimentally determine the viewing region was developed in a previous experiment [6]. A light-emitting diode (LED) is placed on a linear translator and moved along the proton beam, simulating light emission from discrete points along the beam, and observed by a photomultiplier, sensitive to visible light, replacing the EM. A calculation of the viewing region based on known aperture sizes agreed well with this measurement and was used in the fitting function.

B. Polarimeter

1. *Determination of the Stokes parameters*

We experimentally determine the intensity and linear polarization of the Lyman-α radiation emitted from H($n=2$) atoms. The Meuller calculus [19-22] is used to mathematically treat the polarization of the light as it traverses the optical system. Optical elements are represented as 4×4 matrices and a light beam is represented by a four-element vector of Stokes parameters. The Stokes parameters completely describe the polarization of a light beam and are defined as

$$\mathbf{S}=\begin{bmatrix} S_0 \\ S_1 \\ S_2 \\ S_3 \end{bmatrix}=\begin{bmatrix} I_{0^\circ}+I_{90^\circ} \\ I_{0^\circ}-I_{90^\circ} \\ I_{45^\circ}-I_{135^\circ} \\ I_{rh}-I_{lh} \end{bmatrix}, \tag{1}$$

where S_0 may also be presented as $I_{45^\circ}+I_{135^\circ}$ or $I_{rh}+I_{lh}$. The variables I_θ represent the intensity of light linearly polarized at an azimuthal angle of θ depress with respect to the z axis and I_{rh} (I_{lh}) represents the intensity of light having negative (positive) helicity, that is, right (left) handedness.

To determine S_0, S_1, and S_2, we need to measure the intensity of light polarized at 0°, 45°, 90°, and 135°. This is accomplished using a rotatable reflection polarizer whose Mueller matrix is [20]

$$\mathbf{M}_{\text{lin pol}}(0°) = R\begin{bmatrix} 1 & P & 0 & 0 \\ P & 1 & 0 & 0 \\ 0 & 0 & \sqrt{1-P^2}\cos\Delta_r & \sqrt{1-P^2}\sin\Delta_r \\ 0 & 0 & -\sqrt{1-P^2}\sin\Delta_r & \sqrt{1-P^2}\cos\Delta_r \end{bmatrix} . \tag{2}$$

The reflectance R is the ratio of reflected to incident intensity using unpolarized light. The polarization P of the linear polarizer is the value of S_1/S_0 for light reflected from the polarizer with unpolarized light incident. The symbol Δ_r represents the phase difference between the 0° and 90° components of the electric field of the light caused by the reflection. A perfect linear polarizer would have $R=0.5$, $P=1$, and $\Delta_r=0$. In principle, this could be done with a reflection from a plane surface of a dielectric oriented at the Brewster angle. In practice, this is very difficult to achieve in the far ultraviolet (UV) because (i) the short wavelength places great demands upon the polishing of a perfectly flat surface and (ii) most materials have a complex index of refraction in the far UV. (An absorbing medium does not have a Brewster angle.) Because of these limitations, the linear polarizer is only a partial polarizer ($P<1$).

Rotation changes θ, the angle between the proton beam axis (z axis) and the linear polarizer's polarization axis. The variation of θ is shown in Fig. 2 with an orientation of $\theta=0°$. The Mueller matrix for the linear polarizer transforms under rotation as

$$\mathbf{M}_{\text{lin pol}}(\theta)=\mathbf{R}(\theta)\mathbf{M}_{\text{lin pol}}(0°)\mathbf{R}(-\theta) , \tag{3}$$

where the rotation matrix $\mathbf{R}(\theta)$ is

$$\mathbf{R}(\theta)=\begin{bmatrix} 1 & 0 & 0 & 0 \\ 0 & \cos2\theta & -\sin2\theta & 0 \\ 0 & \sin2\theta & \cos2\theta & 0 \\ 0 & 0 & 0 & 1 \end{bmatrix} . \tag{4}$$

In the apparatus, the angle θ is adjustable in 45° steps. Since rotation necessitates breaking vacuum, and since the detector degrades when exposed to air, its detection efficiency will depend on the angle θ (not a functional dependence, but one which change each time the detector is rotated and exposed to air).

The detector acts as an inefficient partial polarizer. The detection efficiency may be represented as a row vector:

$$\varepsilon(\gamma)=\varepsilon_0(\theta)(1 \quad \varepsilon\cos2\gamma \quad \varepsilon\sin2\gamma \quad 0) , \tag{5}$$

where ε_0 is the detection efficiency of the detector for Lyman-α photons and the θ-dependence has been made explicit. The sensitivity of the detector to the linear polarization of the light is represented by ε. The angle between the z axis and the polarization axis of the detector is γ, indicated in Fig. 2. With the linear polarizer at θ and the detector at γ, the measured intensity is

$$\begin{aligned} I_{\theta,\gamma} &= \varepsilon(\gamma)\cdot[\mathbf{M}_{\text{lin pol}}(\theta)\mathbf{S}] \\ &= \varepsilon(\gamma)\cdot[\mathbf{R}(\theta)\mathbf{M}_{\text{lin pol}}(0°)\mathbf{R}(-\theta)\mathbf{S}] , \end{aligned} \tag{6}$$

which can be expanded to

$$\begin{aligned} I_{\theta,\gamma} = \varepsilon_0(\theta)R\{ & S_0 + PS_1\cos2\theta + PS_2\sin2\theta \\ & + \varepsilon\cos(2\gamma)[PS_0\cos2\theta + S_1\cos^2 2\theta + S_1\sqrt{1-P^2}\sin^2 2\theta\cos\Delta_r \\ & + S_2\sin2\theta\cos2\theta(1-\sqrt{1-P^2}\cos\Delta_r) - S_3\sqrt{1-P^2}\sin2\theta\sin\Delta_r] \\ & + \varepsilon\sin(2\gamma)[PS_0\sin2\theta + S_1\sin2\theta\cos2\theta(1-\sqrt{1-P^2}\cos\Delta_r) \\ & + S_2\sin^2 2\theta + S_2\sqrt{1-P^2}\cos^2 2\theta\cos\Delta_r + S_3\sqrt{1-P^2}\cos2\theta\sin\Delta_r]\} . \end{aligned} \tag{7}$$

To simplify this, we first remove the effects of the detector's polarization sensitivity. By setting $\theta=0°$, Eq. (7) becomes

$$\begin{aligned} I_{0°,\gamma} = \varepsilon_0(0°)R\{ & S_0 + PS_1 + \varepsilon(\cos\gamma)(PS_0 + S_1) \\ & + \varepsilon(\sin\gamma)(S_0\cos\Delta + S_3\sin\Delta)\} . \end{aligned} \tag{8}$$

The additional factors in the $\varepsilon(\sin\gamma)$ term make it negligible in comparison with the $\varepsilon(\cos\gamma)$ term. This was confirmed in an experimental test. For $\theta=0°$, we see that $\gamma=45°$ removes the dependence on ε. In general, terms containing ε drop out if $\gamma=\theta+45°$. Setting the detector angle such that $\gamma=\theta+\pi/4$, we simplify the measured intensity for 0°, 45°, 90°, and 135°.

$$\begin{aligned} I_{0°} &= \varepsilon_0(0°)R\{S_{0+} PS_1 + \varepsilon\sqrt{1-P^2}[S_2\cos\Delta_r + S_3\sin\Delta_r]\} , \\ I_{45°} &= \varepsilon_0(45°)R\{S_0 + PS_2 + \varepsilon\sqrt{1-P^2}[S_1\cos\Delta_r \\ &\qquad - S_3\sin\Delta_r]\} , \\ I_{90°} &= \varepsilon_0(90°)R\{S_0 - PS_1 + \varepsilon\sqrt{1-P^2}[S_2\cos\Delta_r \\ &\qquad - S_3\sin\Delta_r]\} , \\ I_{135°} &= \varepsilon_0(135°)R\{S_0 - PS_2 + \varepsilon\sqrt{1-P^2}[S_1\cos\Delta_r \\ &\qquad + S_3\sin\Delta_r]\} , \end{aligned} \tag{9}$$

where the γ subscript has now been dropped. The terms

multiplied by $\varepsilon\sqrt{1-P^2}$ are neglected.

Determining the Stokes parameters S_0, S_1, and S_2 from measurements of the four quantities given in Eq. (9) requires a knowledge of ε_0 at each different θ. Since this is not known, we perform relative measurements at each θ to cancel out the ε_0 factor. Since our intensity measurements are not absolute, we define $S_0(0)=1$. By symmetry, $S_2(0)=0$. With these simplifications, we invert Eq. (9) to obtain the Stokes parameters in terms of the measured relative intensities:

$$
\begin{aligned}
S_0(E)&=\tfrac{1}{2}\{I_{0°_r}(E)[1+PS_1(0)]+I_{90°_r}(E)[1-PS_1(0)]\}\ ,\\
S_1(E)&=\frac{1}{2P}\{I_{0°_r}(E)[1+PS_1(0)]\\
&\qquad -I_{90°_r}(E)[1-PS_1(0)]\}\ ,\\
S_0(E)&=\tfrac{1}{2}\{I_{45°_r}(E)+I_{135°_r}(E)\}\ ,\\
S_2(E)&=\frac{1}{2P}\{I_{45°_r}(E)-I_{135°_r}(E)\}\ .
\end{aligned}
\tag{10}
$$

[Note that the factor of $\frac{1}{2}$ in Eq. (10) differs from the original definitions of the Stokes parameters in Eq. (1) because of the artificially imposed condition $S_0(0)=1$.] Measurements at 0° and 90° will yield S_0 and S_1, while measurements at 45° and 135° will yield S_0 and S_2. Before we can calculate the Stokes parameters from our relative intensity measurements, we need to know P and $S_1(0)$. The determination of $S_1(0)$ is discussed in Sec. III B 2. Figure 3 shows the Stokes parameters S_0, S_1, and S_2 as a function of axial and transverse electric-field strengths for 50-keV proton energy.

In a test to determine P, a perfect linear polarizer ($P=1$) is placed between the glass linear polarizer and the detector. This perfect linear polarizer was not used in the experimental measurements because it has a very small reflectance ($R<1\%$). It consists of four gold (Au) reflectors oriented to produce a 60° angle of incidence. The Au linear polarizer is mounted onto the front of the detector so that they can be rotated together without changing the angle between them. We determine the polarization P of the glass linear polarizer by measuring the light intensity as the Au linear polarizer is rotated with respect to it. The light source is a H_2-filled ionization gauge tube located directly across from the optical chamber. The H_2 gas in the tube is excited by electrons which are emitted in all directions from the tube's filament. The predominant wavelength of emission in the far UV is Lyman-α [23], and the polarization of the light is negligible [24]. Fitting the observed results to an equation obtained from the Mueller matrices for the two polarizers yielded $P=0.81\pm0.2$.

The reflectance R of the glass linear polarizer is estimated by removing the mirror and positioning the detector to intercept directly the light beam from the excited atoms. Comparing the measured intensity in this setup to the measured intensity with the mirror in place allows a rough estimate for R of 25%.

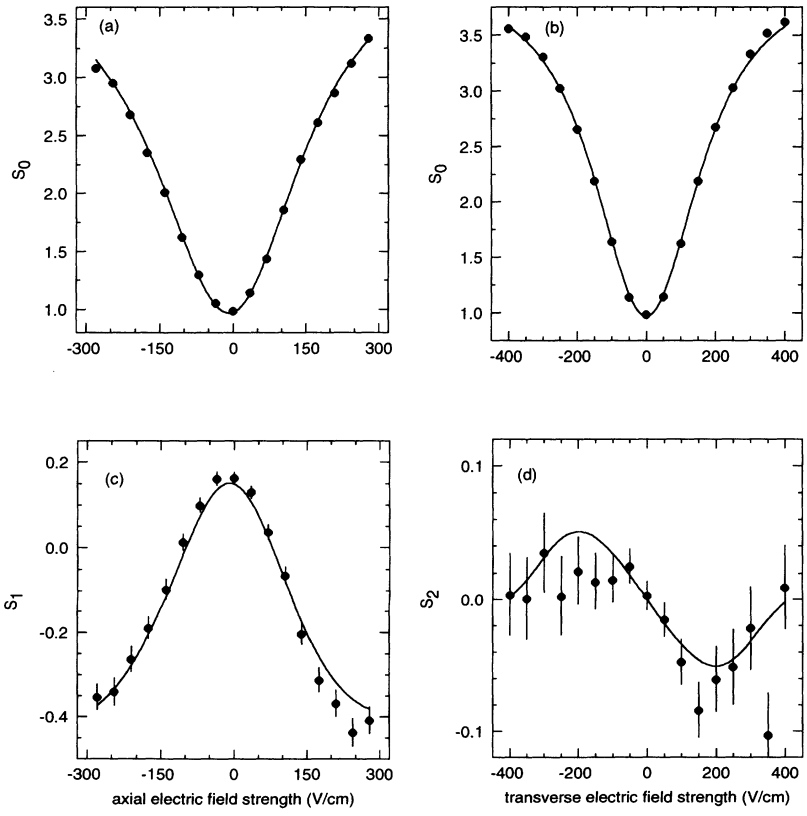

FIG. 3. Stokes parameters $S_i(E)$ for 50 keV proton energy, shown with combined fit.

2. Polarimeter imperfections

We can check the alignment of the optical system with respect to the z axis by taking advantage of the symmetries of the Stokes parameters. For transverse electric fields, S_0 and S_1 are symmetric with respect to zero-electric-field strength and S_2 and S_3 are antisymmetric [25]. A misalignment between the optical system and the z axis would mix the linear polarizations S_1 and S_2. For a small misalignment angle α, the measured S_1' and S_2' (in terms of the source's S_1 and S_2) are

$$\begin{aligned} S_1' &= S_1 + 2\alpha S_2 \ , \\ S_2' &= S_2 - 2\alpha S_1 \ . \end{aligned} \tag{11}$$

Since $S_2 \ll S_1$, the effect on S_1' will be much smaller than the effect on S_2'. If we symmetrize S_2', we find

$$S'_{2\text{symm}} = \tfrac{1}{2}[S_2'(+E) + S_2'(-E)] = -2\alpha S_1(\pm E) \ , \tag{12}$$

where the antisymmetry (symmetry) of S_2 (S_1) has been used. Now if we divide our experimental $S'_{2\text{symm}}$ by the predicted $S_{1\text{fit}}$, we can find α using

$$\alpha = -\frac{1}{2}\left[\frac{S'_{2\text{symm}}}{S_{1\text{fit}}}\right]_{\text{av}} , \tag{13}$$

where the average is taken over all electric-field strengths (transverse-field direction only) and over all energies. The result is $\alpha = 0.89° \pm 1.12°$.

Because the optical system does not contain a wavelength-selective filter, light of all wavelengths between 105 nm (LiF vacuum window cutoff) and 160 nm (approximate limit of detector sensitivity) is detected. Within the considered wavelength range, the Lyman-α measurement may be contaminated by He^+ spectral lines at 164 nm ($n=3 \rightarrow n=2$) and 122 nm ($n=4 \rightarrow n=2$). The detector is ten times more sensitive to 122-nm photons than to 164-nm photons so the $He^+(n=3 \rightarrow n=2)$ transition is ignored. However, any $He^+(n=4)$ ions produced in the collision which then decay to $n=2$ will be detected. An estimate of this contribution, made from other measurements [26] indicates that the largest relative contribution is at higher proton energies, 100 keV in our case. At this energy the cross section for photon emissions from the He^+ (122 nm) transition is roughly three times less than the $H(2p_{\pm 1})$ cross section. It should be noted that χ^2 is largest for the three highest proton energies, possibly indicating a systematic influence from He^+ emission. It is possible to alter the fitting-function program to calculate the fitting function for He^+ emission in an electric field. However, the size of the effect does not justify the amount of effort needed to do the calculation.

The error propagation from $I_{\theta r}(E)$ to $S_i(E)$ uses standard statistical techniques [27] which involve taking derivatives of Eq. (10) with respect to $I_{\theta r}(E)$. Only the results of the error propagation are given here. To simplify the equations, the electric-field dependence is not shown explicitly. Errors in P, $S_1(0)$, and the correction to proton current for axial electric fields are negligible compared to the statistical error in the intensity measurement.

For axial electric fields we know $I_{0°r}$, $I_{90°r}$, $\sigma^2_{I_{0°r}}$, and $\sigma^2_{I_{90°r}}$. The covariance matrix containing the experimental variances and covariances of S_0 and S_1 is

$$\mathbf{C}_{\text{axial}} = \begin{bmatrix} \sigma^2_{S_0} & \sigma^2_{S_0S_1} \\ \sigma^2_{S_0S_1} & \sigma^2_{S_1} \end{bmatrix} . \tag{14}$$

The variances are

$$\begin{aligned} \sigma^2_{S_0} &= \tfrac{1}{4}\{\sigma^2_{I_{0°r}}[1+PS_1(0)]^2 + \sigma^2_{I_{90°r}}[1-PS_1(0)]^2\} \ , \\ \sigma^2_{S_1} &= \frac{1}{4P^2}\{\sigma^2_{I_{0°r}}[1+PS_1(0)]^2 + \sigma^2_{I_{90°r}}[1-PS_1(0)]^2\} \ , \end{aligned} \tag{15}$$

and the covariance term is

$$\sigma^2_{S_0S_1} = \frac{1}{4P}\{\sigma^2_{I_{0°r}}[1+PS_1(0)]^2 - \sigma^2_{I_{90°r}}[1-PS_1(0)]^2\} \ . \tag{16}$$

For transverse electric fields we know $I_{45°r}$, $I_{135°r}$, $\sigma^2_{I_{45°r}}$, and $\sigma^2_{I_{135°r}}$. The covariance matrix containing the experimental variances and covariances of S_0 and S_2 is

$$\mathbf{C}_{\text{transverse}} = \begin{bmatrix} \sigma^2_{S_0} & \sigma^2_{S_0S_2} \\ \sigma^2_{S_0S_2} & \sigma^2_{S_2} \end{bmatrix} . \tag{17}$$

The variances are

$$\begin{aligned} \sigma^2_{S_0} &= \tfrac{1}{4}\{\sigma^2_{I_{45°r}} + \sigma^2_{I_{135°r}}\} \ , \\ \sigma^2_{S_2} &= \frac{1}{4P^2}\{\sigma^2_{I_{45°r}} + \sigma^2_{I_{135°r}}\} \ , \end{aligned} \tag{18}$$

and the covariance term is

$$\sigma^2_{S_0S_2} = \frac{1}{4P}\{\sigma^2_{I_{45°r}} - \sigma^2_{I_{135°r}}\} \ . \tag{19}$$

III. DATA ANALYSIS

A. Fitting functions

The theoretical analysis was developed in a previous experiment [6] to determine the $H(n=3)$ density matrix. A brief outline is given here with emphasis on the differences for $H(n=2)$.

We observe an ensemble of $H(n=2)$ atoms which are produced in collisions having various scattering angles. A convenient formalism [10] describing such an ensemble is the density matrix σ_2, which is shown in Fig. 4. Various symmetries in the experiment [6] limit the number of nonzero independent density-matrix elements to five real parameters: s_0, p_0, $p_{\pm 1}$, $\text{Re}(s_0p_0)$, and $\text{Im}(s_0p_0)$, where the σ designation has been dropped to simplify notation. Note that $p_{\pm 1} = p_{+1} = p_{-1}$, and $\text{Re}(s_0p_0)$ and $\text{Im}(s_0p_0)$ are taken from the upper triangle of the density matrix. The diagonal density-matrix elements represent cross sections for electron transfer into particular $2lm_l$ states. Nondiagonal elements represent coherences between these states, implicitly averaged over scattering angles.

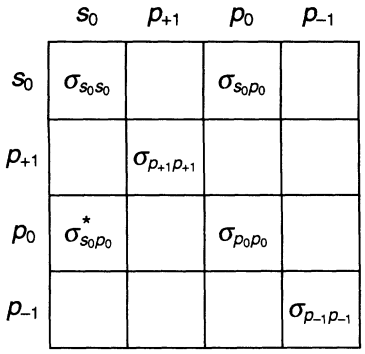

FIG. 4. H($n=2$) density matrix. A blank indicates a density-matrix element which is identically zero due to symmetry.

The density-matrix elements are determined from an analysis of the experimentally determined Stokes parameters, which are a linear combination of contributions from individual density-matrix elements. These individual contributions are referred to as fitting functions. For each density-matrix element there is a fitting function for each Stokes parameter for both electric-field directions. The value of the fitting function for density-matrix element σ_{2jk} at electric-field strength E for Stokes parameter S_i is $f_{ijk}^{(a,t)}(E)$, where the superscript indicates axial or transverse electric-field direction. We also calculate fitting functions for H($n=3$) atoms which cascade through $n=2$ to $n=1$. The H($n=3$) density-matrix element σ_{3jk} produces cascade fitting functions $g_{ijk}^{(a,t)}(E)$ with the same notation as before. Cascade from H($n>3$) is less significant and is therefore neglected.

The fitting functions for a particular density-matrix element are calculated by assuming that element to be the only nonzero element. Doing so produces five basis density matrices which describe the production of H($n=2$) atoms. The fitting-function calculation allows for production of H($n=2$) atoms at all points inside the gas cell. These atoms are time evolved in the presence of an external electric field and their decay to H($n=1$) via electric dipole radiation is calculated at all points within the viewing region from which the Stokes parameters are determined. These calculations are performed on the basis of hyperfine angular momentum states where the Hamiltonian is phenomenological and the radiative decay rates are included as imaginary diagonal terms. Stark interaction terms due to the electric field are included as off-diagonal elements of the Hamiltonian. All of the valid equations for delay of H($n=3\rightarrow n=2$) have been given previously [6]. These same equations are used with the substitution of H($n=2\rightarrow n=1$). The analysis accounts for inhomogeneities in target gas density, electric-field strength, and detection efficiency, as well as the variation of angles of emission from different points inside the viewing region. The cascade fitting functions are calculated analogously, starting with 14 H($n=3$) basis density matrices and calculating their decay through $n=2$ to $n=1$. The analysis assumes that the applied electric field has no effect on the collision process—a valid assumption considering the relative size of the applied electric field and the electric field produced within the collision by the proton and He ion.

B. Fitting procedure

1. General

The purpose of the fitting procedure is to fit statistically the experimentally determined Stokes parameters to the fitting functions, extracting the five unknown density-matrix elements as the coefficients of the fit. Standard statistical methods are used in the fit [27], including the covariance matrix for the measured Stokes parameters. These methods were used in a previous experiment [6].

The five $n=2$ fitting functions $f_{ijk}^{(a,t)}(E)$ are put into the form of a matrix $\mathbf{F}(E)$. For each electric-field strength, the best estimate for the Stokes vector from the fit is related to the density-matrix elements by

$$\mathbf{S}^{\text{fit}}=\mathbf{F}\sigma^{\text{col}} , \tag{20}$$

where σ^{col} contains the density-matrix elements in a column vector. The fitting procedure determines σ^{col} from the measured Stokes vector $\mathbf{S}^{\text{meas}}$ and its associated covariance matrix $\mathbf{C}$ by minimizing the difference between $\mathbf{S}^{\text{fit}}$ and $\mathbf{S}^{\text{meas}}$. The quantity to be minimized in the fit is

$$\chi^2=\sum_{i,j}(\mathbf{S}_i^{\text{meas}}-\mathbf{S}_i^{\text{fit}})\mathbf{W}_{ij}(\mathbf{S}_j^{\text{meas}}-\mathbf{S}_j^{\text{fit}}) , \tag{21}$$

where $\mathbf{W}$ is the inverse of the covariance matrix. This problem has an exact solution and χ^2 is a minimum when

$$\sigma^{\text{col}}=(\mathbf{F}^T\mathbf{W}\mathbf{F})^{-1}\mathbf{F}^T\mathbf{W}\mathbf{S}^{\text{meas}} \tag{22}$$

and

$$\mathbf{C}_{\sigma^{\text{col}}}=(\mathbf{F}^T\mathbf{W}\mathbf{F})^{-1} . \tag{23}$$

$\mathbf{C}_{\sigma^{\text{col}}}$ is the covariance matrix for the density-matrix elements and is used to propagate errors in linear combinations of density-matrix elements.

It is possible to allow each $n=3$ cascade fitting function to vary freely, introducing an additional 14 unknowns to be determined from the fit. This leads to large uncertainties in the $n=3$ density-matrix elements, since the cascade contributions are so small. Instead, the entire $n=3$ density matrix is represented by one fitting function as follows. Since the $n=3$ density matrix is known from previous research, we can construct the following $n=3$ cascade fitting function at each electric-field strength:

$$g_i^{(a,t)}=\sum_{i,j}g_{ijk}^{(a,t)}\sigma_{3jk} , \tag{24}$$

where the $n=3$ density matrix elements σ_{3jk} are normalized to the $\sigma_{3s_0s_0}$ element. The fitting function $g_i^{(a,t)}$ represents the contribution to the Lyman-α signal from all H($n=3$) atoms which cascade through $n=2$ to $n=1$. This fitting function can be used with the five $n=2$ fitting functions in a six-parameter fit or may be combined with

the $2s$ fitting function $f^{(a,t)}_{i;2s_0s_0}$ as follows: To combine the contribution from the $n=3$ manifold with the $2s$ fitting function, we need to know the ratio σ_{3s}/σ_{2s} because the $n=3$ fitting function is normalized to the $\sigma_{3s_0s_0}$ element. The ratio σ_{3s}/σ_{2s} is determined separately (see below). We construct a new $2s$ fitting function,

$$f'^{(a,t)}_{i;s_0s_0}=f^{(a,t)}_{i;s_0s_0}+g^{(a,t)}_i\frac{\sigma_{3s}}{\sigma_{2s}} . \tag{25}$$

This new $2s$ fitting function replaces the old one in the fit, incorporating the correction for cascade from $n=3$, so we have a five-parameter fit to determine the $n=2$ density-matrix elements.

In the axial fit we use the experimental data from axial electric fields—namely, $S_0(E)$ and $S_1(E)$—with axial fitting functions. In the transverse fit we use the experimental data from transverse electric fields—namely, $S_0(E)$, $S_2(E)$, and $S_1(0)$—with transverse fitting functions. Here, $S_1(0)$ supplements the other transverse-field measurements to give a better determination of the $2p$ density-matrix elements. While $S_1(0)$ is not actually measured, it is used in the fit and its assigned standard deviation is the same as the measured standard deviation in $S_0(0)$. All of the above data and their associated fitting functions are used in the combined fit. Figure 3 shows the Stokes parameters with the fitted line from the combined fit to 50-keV data.

2. *Determination of $S_1(0)$*

The combined fit is used to determine $S_1(0)$. An initial value is assigned to $S_1(0)$ in Eq. (10) to determine the Stokes parameters from the relative experimental intensity measurements. The Stokes parameters determined with axial and transverse electric fields are used with their respective fitting functions in a combined fit and χ^2 is noted. Then $S_1(0)$ is varied in steps of 0.001, at each value recalculating the Stokes parameters and repeating the fit, each time noting the value of χ^2. This process continues until the value of $S_1(0)$ is found which produces a minimum in χ^2. This is the experimentally determined value for $S_1(0)$. This value is then used in the separate axial and transverse fits as well as in the combined fit to determine the density-matrix elements. Table I lists the values of $S_1(0)$ versus proton energy.

Figure 5 shows a graph of χ^2 versus $S_1(0)$ for 50-keV combined data. The standard deviation in $S_1(0)$ is determined from the graph [27] by finding the value of $S_1(0)$ where (unreduced) $\chi^2=\chi^2_{\min}+1$. Using this procedure, we find

$$S_1(0)=0.1844\pm0.0067$$

for 50 keV proton energy. The standard deviation in $S_1(0)$ is expected to be nearly the same for all proton energies.

3. *Statistical F tests*

We perform statistical F tests [27] to determine the significance of each of the fitting functions in the fit. An

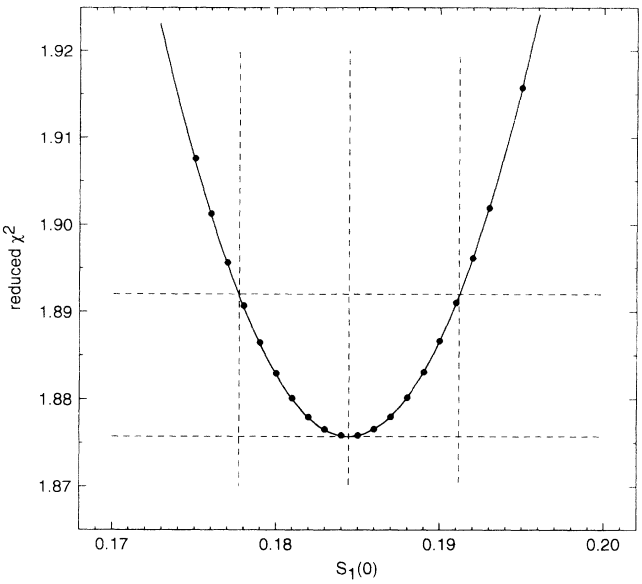

FIG. 5. From 50-keV combined fit, χ^2 versus $S_1(0)$. The dotted lines indicate positions of χ^2_{min} and of $\chi^2_{min}+1$.

F test is a comparison of values of χ^2 from two different fits, one normal and one excluding a single fitting function. The statistical F_χ is defined as

$$F=\frac{\Delta\chi^2}{\chi^2_\nu} , \tag{26}$$

where $\Delta\chi^2$ is the change in the unreduced χ^2 between the two fits and χ^2_ν is the reduced χ^2 for the normal fit. If the considered fitting function is important in the fit, then χ^2 will increase dramatically when it is excluded, producing a large F value. A value of $F<2$ indicates that the inclusion of the considered fitting function in the fit is statistically insignificant. In Table II we show F values from five- and six-parameter fits using combined data from 50 keV proton energy. While the F value for the $\mathrm{Im}(s_0p_0)$ fitting function permits us to exclude it from the fit, its physical significance requires us to include it, at least in certain cases. When the $\mathrm{Im}(s_0p_0)$ fitting function is included in axial data fits, its standard deviation is never less than 1.2, whereas its absolute value, from combined fitting, never exceeds 0.7. In transverse and combined

TABLE I. Values of $S_1(0)$ for all proton energies.

Proton energy (keV)	$S_1(0)$
20	0.090
25	0.174
30	0.188
35	0.196
40	0.202
50	0.184±0.007
50	0.193
60	0.190
80	0.150
100	0.157

TABLE II. Results from F tests using five- and six-parameter fits.

Fitting function excluded	χ_ν^2	F
None (five parameters)	1.88	
s_0	1343	46 000
$\mathrm{Re}(s_0p_0)$	11.5	327
$\mathrm{Im}(s_0p_0)$	1.80	<0
p_0	32.7	1049
$p_{\pm1}$	7.6	195
None (six parameters)	1.83	
Cascade	2.05	8.5

fitting, however, including the $\mathrm{Im}(s_0p_0)$ fitting functions produces significant results, with the standard deviation typically being smaller than the absolute value of the parameter. Therefore, we include the $\mathrm{Im}(s_0p_0)$ fitting function in transverse and combined fits but exclude it from axial fits. While the F value for the cascade fitting function is statistically significant, six-parameter fits including it indicate an absolute value comparable to its standard deviation. Since it is possible to determine σ_{3s}/σ_{2s} from the experiment, it is more reasonable to add the cascade fitting function (scaled by σ_{3s}/σ_{2s}) to the s_0 fitting function and then to perform five-parameter fits.

4. *Evaluation of errors*

The statistical fits provide error estimates for the density-matrix elements. The source of these errors is the counting statistics of the initial intensity measurements. Because there are sources of experimental error other than counting statistics, the standard deviations of the Stokes parameters are underestimated, causing χ^2 to be greater than unity in the fits. Table III shows the values for χ^2 from combined, axial, and transverse fits. To provide a better estimate of the experimental error, the covariance matrix for the density-matrix elements is multiplied by χ^2. Note that outlying points (more than ten standard deviations from the fitted line) are automatically discarded. This amounts to less than 1% of the experimental data.

A test of the validity of multiplying the covariance matrix of the density-matrix elements by χ^2 is possible because of the symmetry of the Stokes parameters. For transverse electric fields we know that S_0 should be symmetric with respect to zero-electric-field strength. We can compare the difference between S_0 with positive and negative electric-field strengths to the standard deviation for S_0, calculating a quantity analogous to χ^2. Doing so yields a value of 2.2 for the reduced sum of the square of the difference divided by the standard deviation. This quantity is to be compared with the average $\chi^2=2.7$ for transverse fits. The nearness of these two numbers indicates that it is valid to multiply the covariance matrix of the density-matrix elements by χ^2.

TABLE III. Values of χ^2 from combined, axial, and transverse fitting.

Energy (kev)	$\chi^2_{\mathrm{combined}}$	χ^2_{axial}	$\chi^2_{\mathrm{transverse}}$
20	2.54	1.21	4.01
25	1.86	1.89	1.68
30	1.76	1.55	1.92
35	1.78	1.70	1.64
40	1.99	1.37	2.20
50	1.88	1.41	1.87
50	2.07	1.32	2.80
60	3.15	1.45	4.09
80	2.98	1.47	3.88
100	3.14	1.34	3.39

To evaluate critically the standard deviations of the density-matrix elements, a variety of fits are performed using fitting functions with different values for the following experimental parameters: width of the viewing region, distance from the entrance plate to the center of the viewing region, and variation of the optical detection efficiency within the viewing region. The width of the viewing region is changed by ±1 mm. The distance from the entrance plate to the viewing region is changed by ±0.5 mm. The optical detection efficiency is varied linearly by $\pm25\%$ within the viewing region. For each of these cases the combined 50-keV data are fit using the altered fitting function, and the change in the density-matrix elements from normal fitting is noted. The largest such change for each density-matrix element is compared with its error estimate from the previous paragraph. Changing the width of the viewing region has the least effect on the fit, while changing the optical detection efficiency within the viewing region has the greatest effect. The largest change in the density-matrix elements relative to their standard deviations is 2.9 for $\mathrm{Re}(s_0p_0)$, 0.6 for $\mathrm{Im}(s_0,p_0)$, 2.2 for p_0, and 2.5 for $p_{\pm1}$. It is not possible to gauge the effect on s_0 since the density matrix is always normalized to s_0; however, its behavior should be similar to the other even-parity elements. To provide a more accurate estimate of the standard deviations of the density-matrix elements, we multiply the standard deviations for the s_0, $\mathrm{Re}(s_0p_0)$, p_0 and $p_{\pm1}$ by 2.5. The $\mathrm{Im}(s_0p_0)$ standard deviation is not adjusted.

As an additional test, the following parameters are changed by one standard deviation to judge the effect on the fit: the polarization P of the reflection polarizer, the variation of proton current with axial electric field, and the ratio σ_{3s}/σ_{2s} used to scale the cascade fitting function. None of these changes has a significant effect on the density-matrix elements. Changing $S_1(0)$ by one standard deviation changes p_0 and $p_{\pm1}$ by one standard deviation.

5. *Determination of σ_{3s}/σ_{2s} and σ_{2s}*

During the time it takes to acquire data for all of the proton energies, there is a drift in the detection efficiency of the optical system. This means that our measurements should not be compared between different proton energies on an absolute scale. For this reason the determined destiny matrices from each proton energy are normalized to the $2s$ element. Since all of the determined $n=2$ density matrices are normalized to the $2s$ element, we have no information about the variation of the electron-

transfer cross section σ_{2s} with energy. The experimental technique to determine σ_{2s} as a function of proton energy was developed previously to determine the energy dependence of σ_{3s} [28]. Using measurements of $S_0(\pm 400$ V/cm) as a function of proton energy for transverse electric fields with the transverse fitting functions and with the density matrices determined from combined fitting, we determine σ_{2s} as a function of proton energy.

The scale for the cross sections is arbitrary since we do not perform absolute intensity measurements. To bring our σ_{2s} cross-section measurements onto an absolute scale, we normalize them to an absolute measurement. For this purpose we use our previously determined σ_{3s} cross sections which were brought onto an absolute scale by normalization to an absolute measurement of σ_{3s} at 60 keV [29]. We form the ratio σ_{3s}/σ_{2s} where σ_{2s} is on an arbitrary scale and require that the ratio should approach a limit of $2^3/3^3=0.296$ as the energy increases. The n^{-3} dependence of cross sections is a well-known result from the Born-Oppenheimer approximation at high energies [30]. The ratio is fit to an empirical model of the form

$$\sigma_{3s}/\sigma_{2s} = A[0.296 - B/(T^C - D)] ,$$

where T is the kinetic energy of the proton in the collision. The value of A from the fit is used to normalize properly the σ_{2s} cross section to bring it onto an absolute scale. This also provides a determination of σ_{3s}/σ_{2s} for lower energies where the cross-section ratio deviates from the n^{-3} scaling law. The energy-dependent σ_{2s} can also be used to normalize properly the energy-dependent density matrices, which are all relative to σ_{2s}.

IV. RESULTS

A. Tabular results

The density-matrix elements from the fits are shown in Table IV. For each element the values and standard deviations are shown for the combined data fit, the axial data fit, and the transverse data fit. The standard deviations have been adjusted as discussed above. The axial and transverse determinations agree, all diagonal elements are positive, and the Schwartz inequality [31] for the s_0p_0 element is obeyed. This indicates that the results

TABLE IV. Density-matrix elements from combined (c), axial (a), and transverse (t) fitting.

Energy (keV)	Fitting	s_0	Re(s_0p_0)	Im(s_0p_0)	p_0	$p_{\pm 1}$
20	c	1.000±0.063	−0.03±0.28	−0.68±0.36	0.954±0.039	0.567±0.031
	a	1.000±0.067	−0.03±0.21		0.975±0.029	0.584±0.025
	t	1.00±0.11	0.3±1.4	−1.03±0.75	0.93±0.16	0.56±0.11
25	c	1.000±0.032	0.16±0.13	−0.54±0.19	0.606±0.020	0.219±0.015
	a	1.000±0.053	0.19±0.15		0.630±0.022	0.236±0.018
	t	1.000±0.042	0.11±0.054	−0.44±0.29	0.593±0.062	0.204±0.041
30	c	1.000±0.020	0.243±0.075	−0.43±0.12	0.384±0.011	0.131±0.009
	a	1.000±0.030	0.258±0.076		0.392±0.012	0.132±0.010
	t	1.000±0.029	0.38±0.37	−0.56±0.20	0.388±0.038	0.124±0.025
35	c	1.000±0.016	0.208±0.057	−0.162±0.097	0.280±0.008	0.091±0.006
	a	1.000±0.025	0.210±0.059		0.289±0.009	0.088±0.007
	t	1.000±0.020	0.30±0.26	−0.25±0.15	0.286±0.023	0.086±0.015
40	c	1.000±0.015	0.275±0.051	−0.148±0.096	0.224±0.008	0.063±0.006
	a	1.000±0.020	0.288±0.046		0.230±0.007	0.067±0.006
	t	1.000±0.021	0.24±0.26	−0.11±0.15	0.216±0.022	0.062±0.015
50	c	1.000±0.011	0.272±0.037	−0.156±0.071	0.158±0.006	0.054±0.004
	a	1.000±0.017	0.284±0.035		0.164±0.006	0.057±0.004
	t	1.000±0.015	0.26±0.17	−0.14±0.11	0.158±0.014	0.050±0.009
50	c	1.000±0.013	0.274±0.043	−0.072±0.079	0.161±0.007	0.052±0.005
	a	1.000±0.018	0.281±0.037		0.167±0.006	0.052±0.004
	t	1.000±0.019	0.22±0.22	0.00±0.14	0.163±0.018	0.048±0.012
60	c	1.000±0.014	0.278±0.042	−0.105±0.087	0.144±0.006	0.041±0.005
	a	1.000±0.016	0.290±0.031		0.147±0.005	0.044±0.004
	t	1.000±0.021	0.27±0.23	−0.10±0.15	0.135±0.018	0.042±0.012
80	c	1.000±0.014	0.279±0.039	0.040±0.082	0.107±0.006	0.045±0.004
	a	1.000±0.017	0.286±0.029		0.109±0.005	0.047±0.004
	t	1.000±0.020	0.21±0.20	0.12±0.13	0.105±0.016	0.042±0.011
100	c	1.000±0.015	0.269±0.042	0.142±0.082	0.108±0.007	0.040±0.005
	a	1.000±0.018	0.272±0.029		0.108±0.005	0.044±0.004
	t	1.000±0.020	0.20±0.18	0.23±0.12	0.103±0.015	0.040±0.010

TABLE V. Absolute cross section σ_{2s} and the ratio σ_{3s}/σ_{2s}.

Energy (keV)	σ_{2s} (10^{-18} cm^2)	σ_{3s}/σ_{2s}
20	2.66±0.14	
25	4.63±0.25	0.148±0.009
30	6.74±0.35	0.180±0.011
35	8.14±0.43	0.203±0.012
40	8.85±0.48	0.221±0.013
50	8.48±0.46	0.252±0.016
50	8.50±0.46	0.252±0.016
60	7.62±0.43	0.262±0.017
80	5.00±0.26	0.283±0.019
100	3.19±0.17	0.285±0.019

are self-consistent.

General trends are that the even-parity elements are best determined from axial data. Axial data also produces better results for $\mathrm{Re}(s_0p_0)$ but transverse data are needed to determine $\mathrm{Im}(_0p_0)$. The diagonal elements obey $s_0>p_0>p_{\pm1}$ at all proton energies, showing a tendency of electron capture toward states of low angular momentum.

The absolute cross section σ_{2s} and the ratio σ_{3s}/σ_{2s} are shown in Table V. The relative density-matrix elements in Table IV were multiplied by σ_{2s} to find their energy-dependent behavior. The error in the absolute value of these cross sections is limited by the 20% error in the original absolute measurement [29].

B. Graphical results

The density matrix may be interpreted [1,3], as defining a charge-density distribution $D(\mathbf{r})$ and a current density distribution [3,32] $\mathbf{j}(\mathbf{r})$ for the electron in the H($n=2$) atom. These distributions provide a graphical view of the H($n=2$) atom at the time of its formation. Figures 6 and 7 display $D(\mathbf{r})$ and $\mathbf{j}(\mathbf{r})$ for different proton energies. Figure 6 shows a clear asymmetry in the electronic charge-density distribution, indicating a nonzero electric dipole moment. This is due to the influence of the product He^+ ion during the collision, which pulls the electron back between the projectile and target nuclei. Figure 7 indicates a change in direction of current flow in the atom around 70 keV, with the largest current flow at 25 keV. These observations are confirmed by calculating the expectation values of various operators of physical significance.

The density-matrix elements, diagonal and nondiagonal, respectively, describe populations of and coherences between angular momentum eigenstates of the H($n=2$) atom. While the density-matrix elements provide a complete description of the H($n=2$) atom, they have little physically intuitive meaning. Instead, density-matrix elements are often combined in physically meaningful combinations which offer some insight into the collision process. Various parameterizations have been suggested [33–35].

We compare our results to the results of other experimental research. There are several measurements of σ_{2s} and σ_{2p}, to be discussed below. Measurements of σ_{2p_m} and off-diagonal density-matrix elements are fewer and more recent, because they are more difficult to determine. Hippler *et al.* [26] and Teubner *et al.* [26] have measured the linear polarization of Lyman-α radiation over a wide range of proton energies between 1 and 300 keV. This measurement is related to a combination of $2p_0$ and $2p_{\pm1}$ cross sections. In addition, using our method, Hippler *et al.* [27,38] have determined the complete H($n=2$) density matrix for proton energies between 5 and 25 keV. The method of DeSerio *et al.* [15] detects Lyman-α quantum beats in the presence of an external electric field. By assuming values for σ_{2s} and σ_{2p_m}, the values of $\mathrm{Re}(s_0p_0)$ and $\mathrm{Im}(s_0p_0)$ are determined for proton energies between 135 and 235 keV.

We also make comparison with the theoretical calculations of Slim *et al.* [39], Shingal and Lin [40], Jain, Lin, and Fritsch [41], and Dubé [42]. Slim *et al.* use the semiclassical impact parameter method with a basis set of traveling atomic orbitals centered on the target and on the projectile. Their calculations are able to treat the helium target as a two-electron atom, whereas all of the other calculations assume only one electron is active in the collision. Shingal and Lin and Jian, Lin, and Fritsch both use the atomic-orbital plus method. Jain, Lin, and Fritsch use a fairly small basis set supplemented by pseudostates, while Shingal and Lin use a much larger basis set. Dubé uses the continuum distorted wave–post collision interaction (CDW-PCI) theory, a high-energy approximation which produces some relevant results for the considered energy range.

Using the density-matrix elements from combined fitting, we calculate various quantities to aid our understanding of the collision process. The electric dipole moment of the H($n=2$) atoms is given by

$$\langle \mathbf{d} \rangle_z = \frac{6\,\mathrm{Re}(s_0p_0)}{\mathrm{Tr}(\sigma_2)} , \tag{27}$$

where $\mathrm{Tr}(\sigma_2)$ is the trace of the H($n=2$) density matrix. From Fig. 8 we see that positive values for the electric dipole moment agree with our interpretation of the asymmetry in the charge-density distribution. Comparison with other experimental research is very good, but theoretical calculations provide only qualitative estimates of the energy dependence of the electric dipole moment. In particular, the CDW-PCI approximation of Dubé greatly underestimates the magnitude of $\langle \mathbf{d} \rangle_z$.

A first-order moment of the current distribution which is proportional to the current flow in the z direction far from the z axis is given by

$$\langle \mathbf{L}\times\mathbf{A} \rangle_{z,s} = \frac{-2\,\mathrm{Im}(s_0p_0)}{\mathrm{Tr}(\sigma_2)} . \tag{28}$$

The vector $\mathbf{L}\times\mathbf{A}$ is proportional to the integral of $\mathbf{r}\times(\mathbf{r}\times\mathbf{j})$ over the entire atom. From Fig. 9 we see that our observations about the magnitude and change in direction of the current flow are confirmed. The comparison with other experiments is good for higher energies, but there is no agreement at lower energies. The alignment A_{20} of the p states (see Fig. 10) is proportional to the electric quadrupole moment of the atom [for H($n=2$)] and is given by

$$A_{20}=\frac{p_{\pm 1}-p_0}{p_0+2p_{\pm 1}} . \tag{29}$$

Our measurements compare favorably with the measurements of Hippler *et al.* [26] and Teubner *et al.* [36] but there is no consensus among theoretical calculations. A measure of how nearly the Schwartz inequality [8] is exceeded is given by the coherence parameter $R_{s_0p_0}$,

$$R_{s_0p_0}=\frac{|\sigma_{s_0p_0}|}{\sqrt{\sigma_{s_0s_0}\sigma_{p_0p_0}}} . \tag{30}$$

Values for $R_{s_0p_0}$ near unity in Fig. 11 indicate that the phase difference between the s_0 and p_0 states remains nearly constant in the implicit average over scattering angles. The agreement with lower-energy measurements is good, but among the theoretical calculations only those of Shingal and Lin show the correct energy dependence. The average coherences [8] $\mathrm{Tr}(\rho^2)$ of the entire density matrix is equal to $\mathrm{Tr}(\sigma_2^2)$ when $\mathrm{Tr}\sigma_2=1$ and is a measure of how nearly the density matrix approximates a pure state. In general, the average coherence for an unnormalized density matrix is

$$\mathrm{Tr}(\rho^2)=\frac{\mathrm{Tr}(\sigma_2^2)}{(\mathrm{Tr}\sigma_2)^2} . \tag{31}$$

The range of values for $\mathrm{Tr}(\rho^2)$ are from $\frac{1}{4}$ for a completely incoherent state to unity for a completely coherent

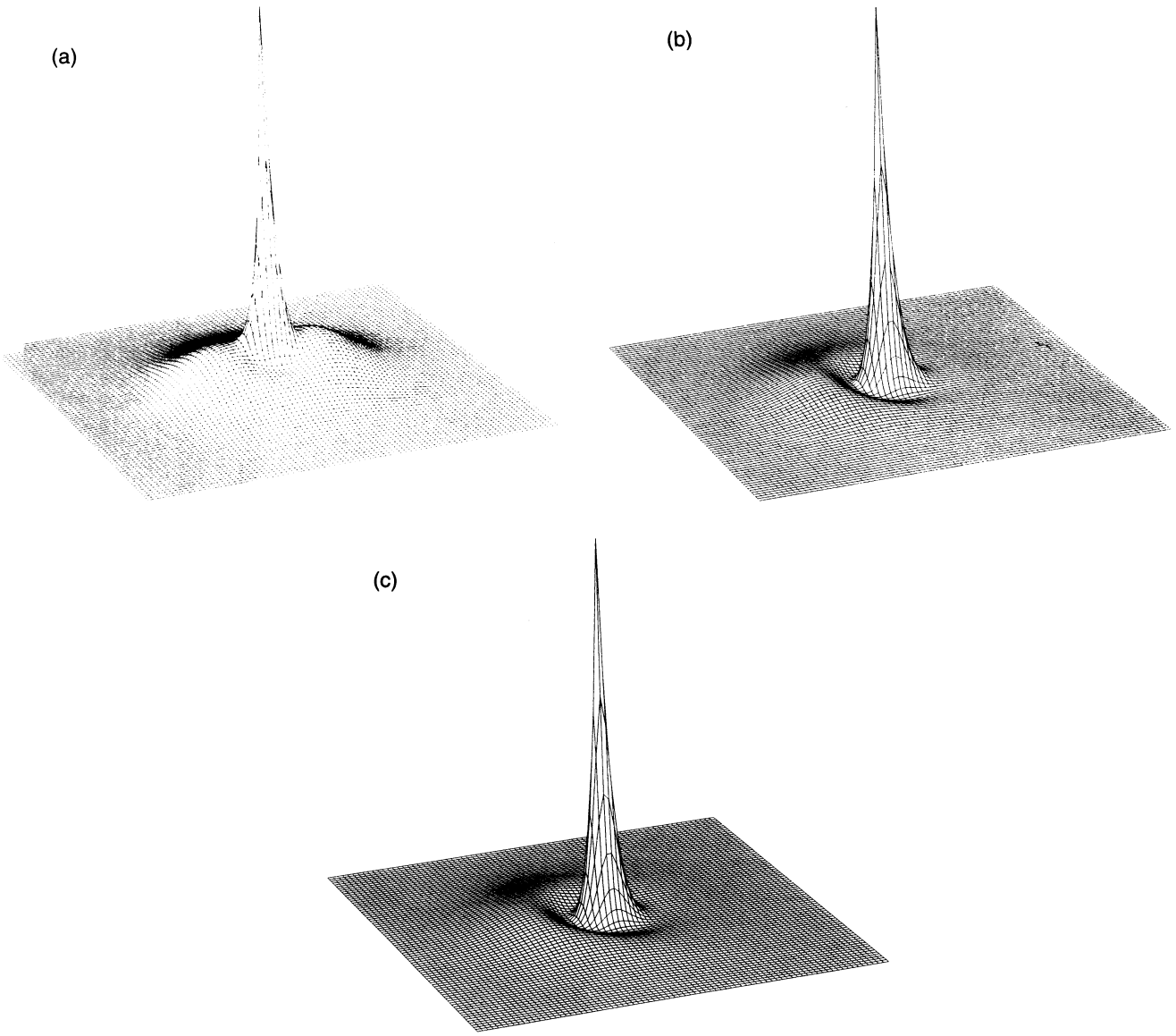

FIG. 6. Electronic charge-density distribution $D(\mathbf{r})$ for the H($n=2$) atoms. In this display the atoms are moving toward the right. The height indicates the probability to find the electron at that position in the xz plane. The scale is between ± 10 atomic units in each direction. (a) 20, (b) 40, and (c) 100 keV.

state. The high values for $\mathrm{Tr}(\rho^2)$ in Fig. 12 at higher proton energies indicate the dominance of the $2s$ state at those energies. For lower proton energies lower values for the average coherence near its lower limit indicate that, in the average over impact parameter, the state of the

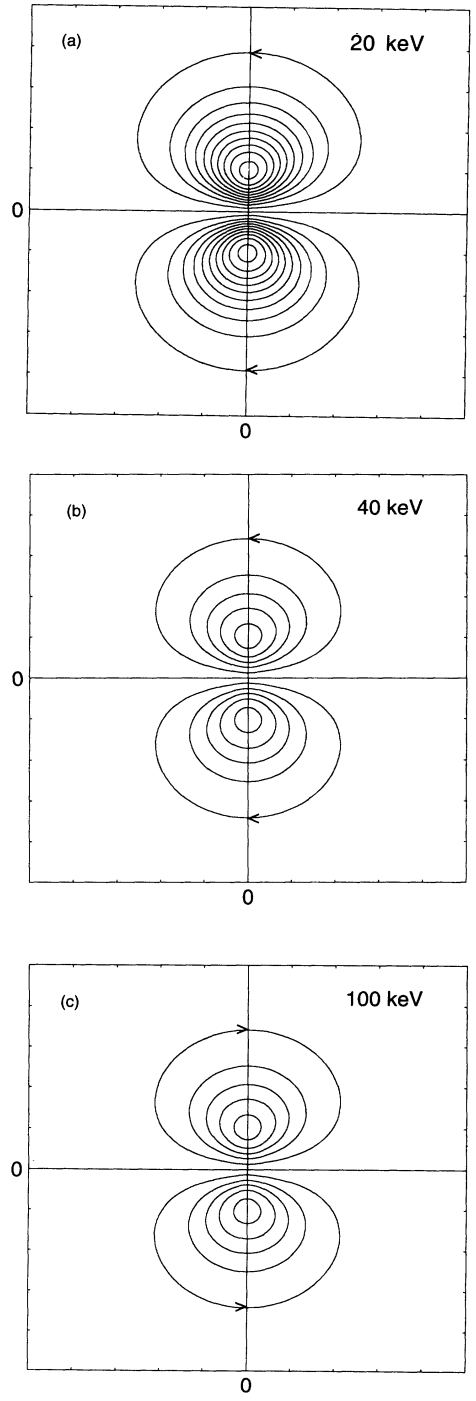

FIG. 7. Electronic current-density distribution $\mathbf{j}(\mathbf{r})$ for the H($n=2$) atoms. In this display the atoms are moving toward the right. The horizontal axis is the z axis and the vertical indicates the distance from the z axis. Each graph shows the region between ± 5 atomic units. (a) 20, (b) 40, and (c) 100 keV.

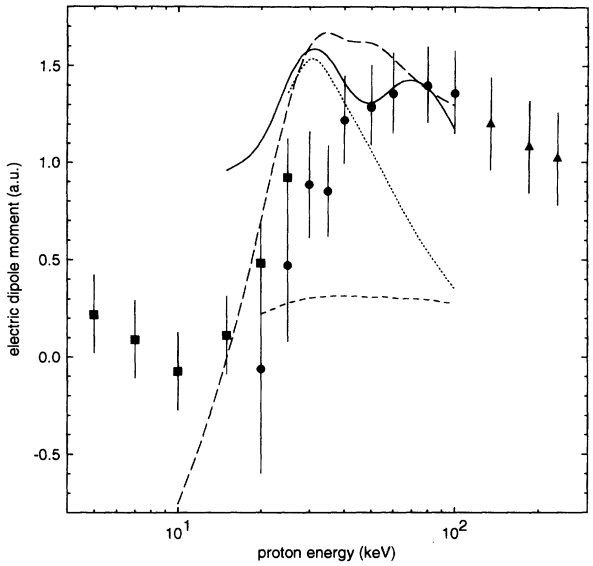

FIG. 8. Electric dipole moment $\langle \mathbf{d} \rangle_z$ of the H($n=2$) atoms. The symbols are as follows: ●, present results; ●, Hippler *et al.* [37,38]; ▲, DeSerio *et al.* [15]; · · · · Jain, Lin, and Fritsch [41]; – – –, Dubé [42]; — — —, Slim *et al.* [39]; and ——, Shingal and Lin [40].

H($n=2$) atoms varies greatly. All of the theoretical calculations predict the same energy dependence, but there is no quantitative agreement between theory and experiment.

For completeness we also show in Fig. 13 the ratio σ_{2s}/σ_{2p} in comparison with measurements of Hippler *et al.* [26] and the various theories. This graph shows more clearly the dominance of electron transfer to states of lower angular momentum at higher proton energies.

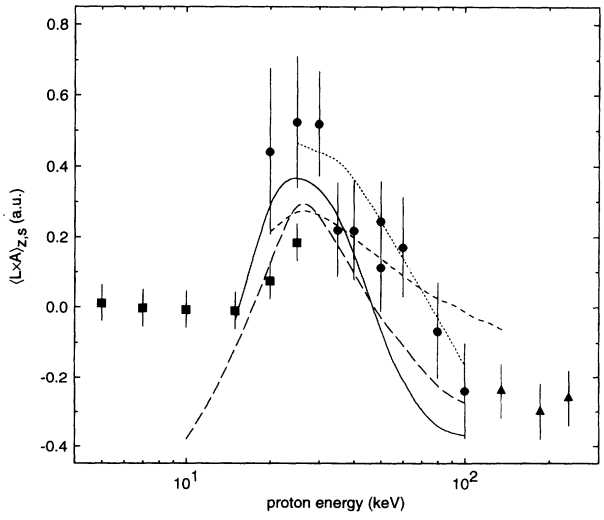

FIG. 9. First-order moment $\langle \mathbf{L} \times \mathbf{A} \rangle_{z,s}$ of $\mathbf{j}(\mathbf{r})$. The symbols are the same as those in Fig. 8.

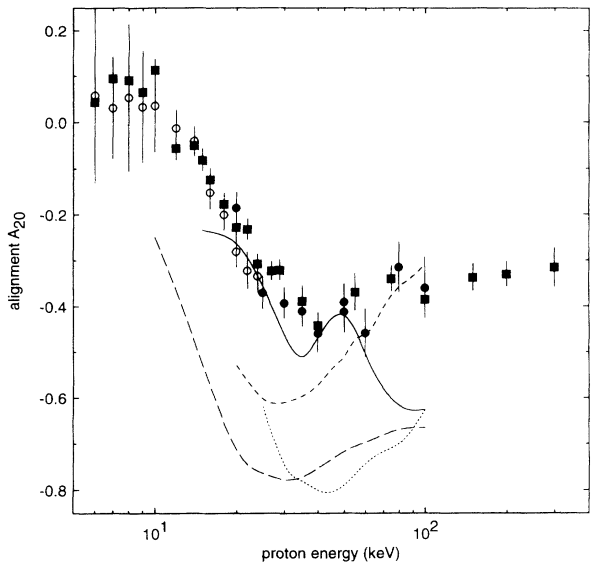

FIG. 10. Alignment A_{20} of the p states of H($n=2$). The symbols are the same as those in Fig. 8 with the addition of ○, Teubner *et al.* [36].

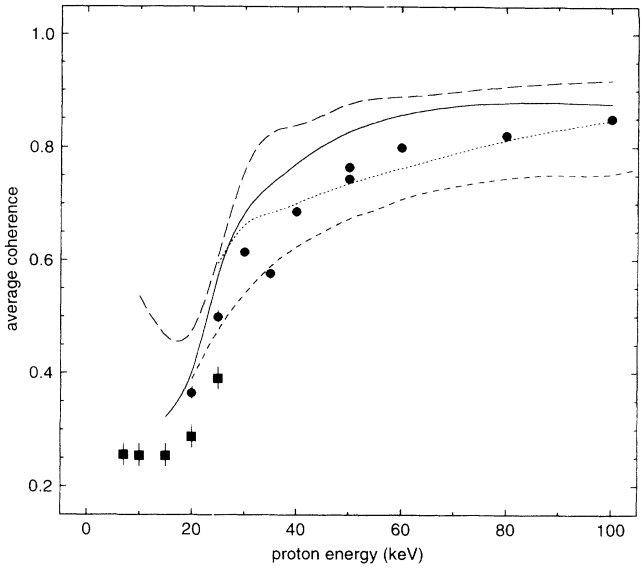

FIG. 12. Average coherence $\mathrm{Tr}(\rho^2)$ of H($n=2$). The symbols are the same as those in Fig. 8.

C. Absolute cross sections

There are numerous measurements of the cross sections σ_{2s} and σ_{2p} [43]. In the older experimental methods, the proton current, He gas density, and absolute light intensity emitted from excited H($n=2$) atoms are measured to compute the cross sections. Quench electric fields are used to observe H($2s$) atoms. Most of the studies ignore polarization effects and make no correction for cascade from higher-lying states [44-51]. Some of those using electric fields to observe radiation from H($2s$) atoms neglect the effect of the electric fields on H($2p$) atoms [44,46,49]. For these reasons these studies are not used for comparison. The only older experiment where some correction is made for all of the above effects is that of Hughes *et al.* [52]. Figure 14 shows the absolute σ_{2s} cross sections, and Fig. 15 shows the absolute and σ_{2p} cross sections as a function of proton energy. The agreement with Hippler *et al.* [38] is good, as is the agreement with Hughes *et al.* above 50 keV. Below that

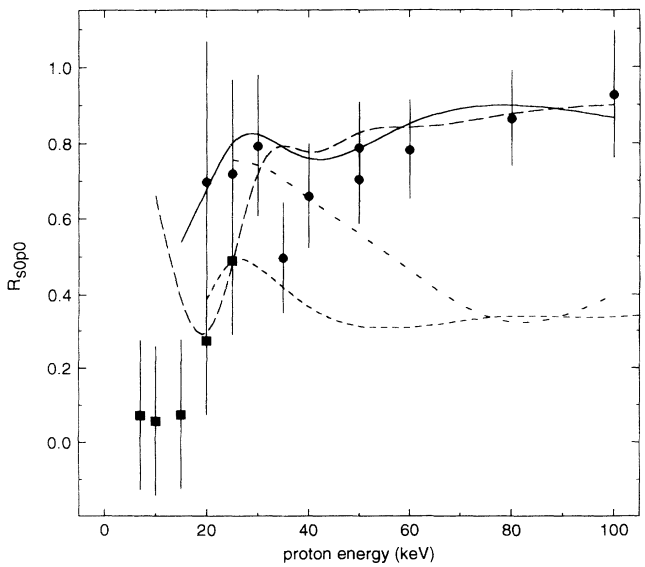

FIG. 11. Coherence parameter $R_{s_0p_0}$. The symbols are the same as in Fig. 8.

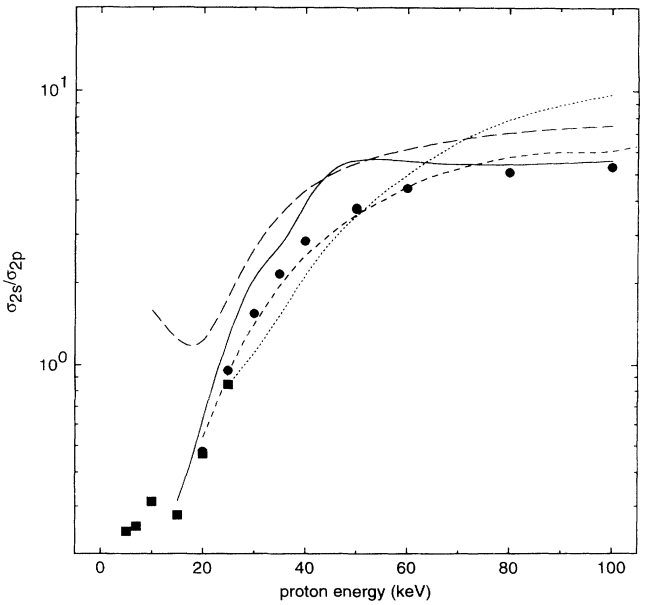

FIG. 13. Cross-section ratio σ_{2s}/σ_{2p}. The symbols are the same as those in Fig. 8.

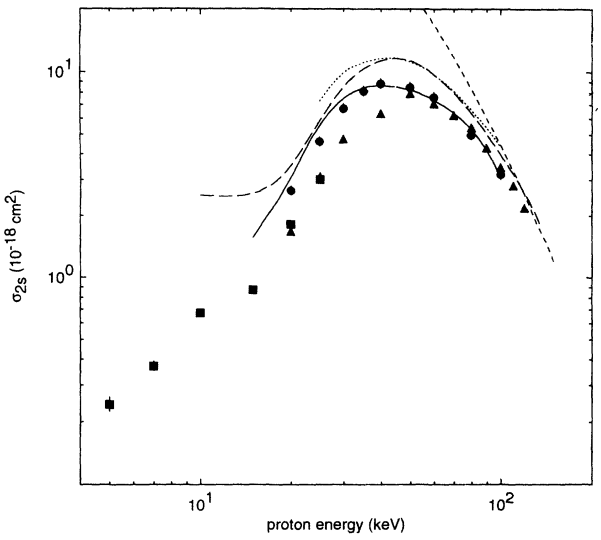

FIG. 14. Absolute cross sections σ_{2s}. The symbols are as follows: ●, $2s$ (present results); ■, $2s$ (Hippler *et al.* [38]); ▲, $2s$ (Hughes *et al.* [52]); ○, $2p$ (present results); □, $2p$ (Hippler *et al.* [38]); △, $2p$ (Hughes *et al.* [52]). One standard deviation for the present results is nearly the size of the symbols.

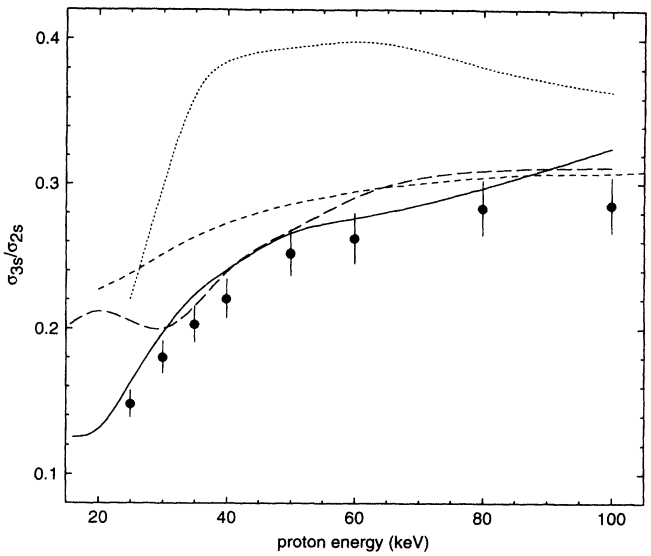

FIG. 16. Ratio of σ_{3s} to σ_{2s}. The symbols are the same as those in Fig. 14.

energy the disagreement is undoubtedly due to the cascade correction of Hughes *et al.*, who assumed n^{-3} scaling [30] for low proton energies.

The scaling between σ_{3s} and σ_{2s} is shown in Fig. 16 where it can be seen that n^{-3} scaling is only valid for energies beyond 100 keV. The best theoretical predictions of Figs. 14–16 are those of Shingal and Lin [40]. While most of the other theories predict the correct qualitative behavior, only Shingal and Lin predict the quantitative variation of these quantities.

D. Comparison of H($n=2$) and H($n=3$)

Using previous density-matrix results [8] for H($n=3$), we can now investigate the n dependence of various collision parameters. Since the angular momentum vector **L** and the Runge-Lenz vector [53] **A** are constants of the motion for hydrogenic systems [35], it is appropriate to compare expectation values of combinations of these operators between different n manifolds [54,55].

The ratio σ_{3p}/σ_{2p}, shown in Fig. 17, approaches a 100-keV limit of about 0.23, contradicting a model [56]

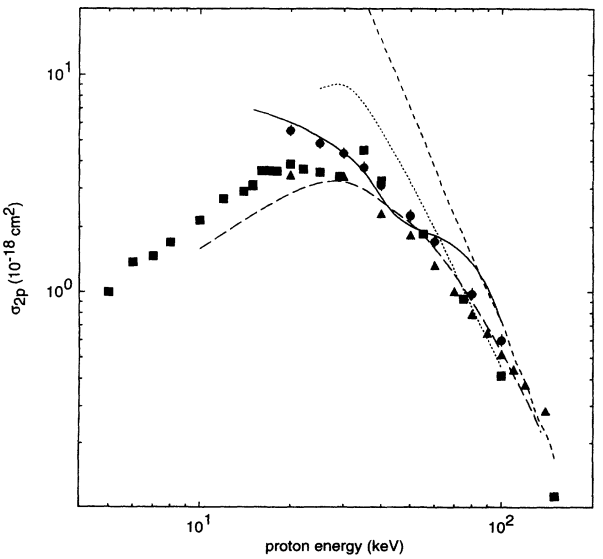

FIG. 15. Absolute cross sections σ_{2p}. The symbols are the same as those in Fig. 14.

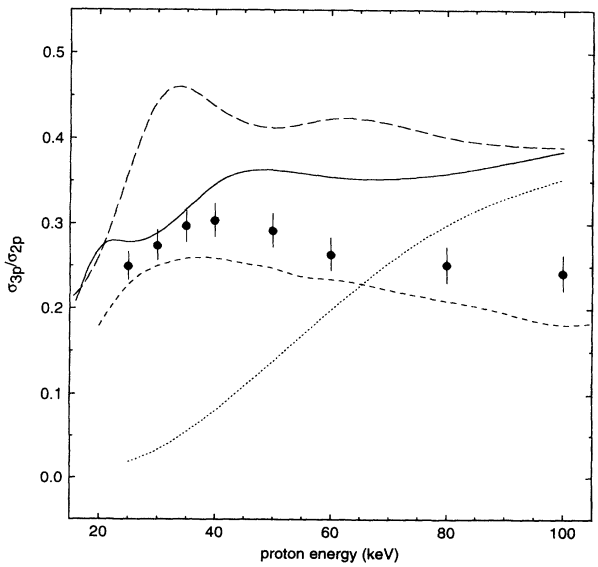

FIG. 17. Cross-section ratio σ_{3p}/σ_{2p}. The symbols are the same as in Fig. 8.

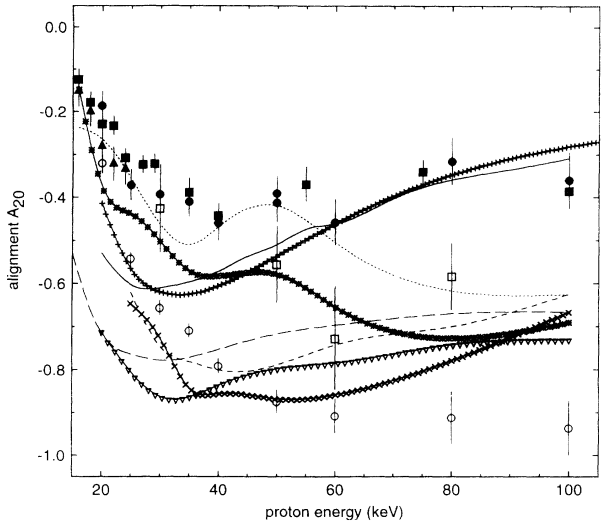

FIG. 18. Alignment A_{20}. The symbols are as follows: ●, $n=2$ (present results); ■, $n=2$ (Hippler *et al.* [37,38]); ▲, $n=2$ (Teubner *et al.* [36]); ○, $n=3$ (Ashburn *et al.* [8]); □, $n=3$ (Brower and Pipkin [29]); ——, $n=2$, (Dubé [42]); · · · ·, $n=2$ (Shingal and Lin [40]); − − −, $n=2$ (Jain, Lin, and Fritsch [41]); — — —, $n=2$ (Slim *et al.* [39]); + + + +, $n=3$ (Dubé [42]); × × × ×, $n=3$ (Jain, Lin, and Fritsch [41]); ****, $n=3$, (Shingal and Lin [40]); ▽▽▽▽, $n=3$ (Slim *et al.* [39]).

for scaling of σ_{nl} which predicts $\sigma_{3p}/\sigma_{2p}=0.35$. Comparison with other experimental research [56–60] is difficult since absolute cross sections have typical errors of 20%, making cross-section ratios very uncertain.

The p-state alignment A_{20} is shown for $n=2$ and 3 in Fig. 18. The difference between the $n=2$ and 3 measurements is surprising since all theories predict the same

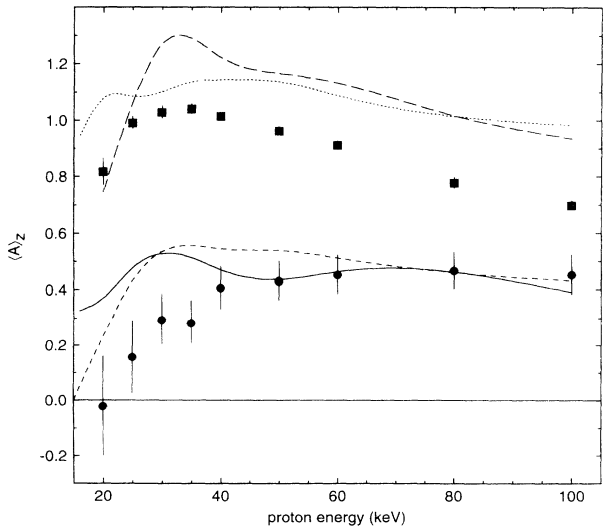

FIG. 19. Dependence of $\langle \mathbf{A} \rangle_z$ on n. The symbols are as follows: ●, present $n=2$ results; ■, $n=3$ (Ashburn *et al.* [8]); ——, $n=2$, and · · · ·, $n=3$ (Shingal and Lin [40]); − − −, $n=2$, and — — —, $n=3$ (Slim *et al.* [39]).

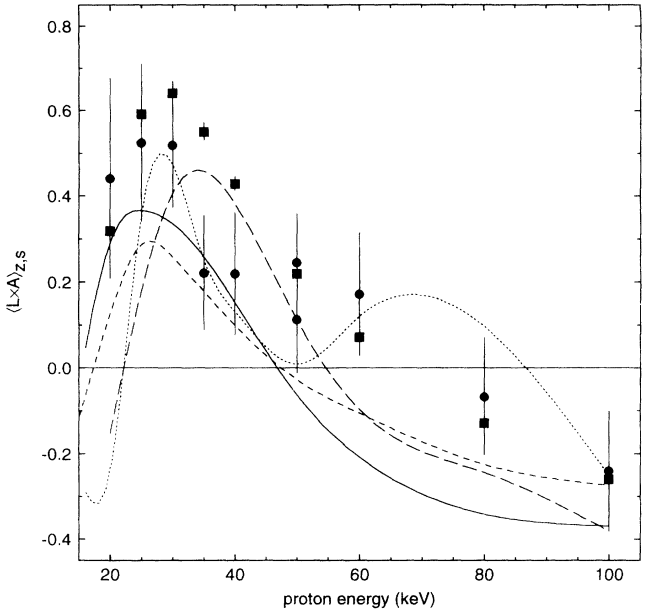

FIG. 20. Dependence of $\langle \mathbf{L} \times \mathbf{A} \rangle_{z,s}$ on n. The symbols are the same as in Fig. 19.

value for the alignment regardless of n at sufficiently high energy in the range investigated here.

The n dependence of $\langle \mathbf{A} \rangle_z$ and $\langle \mathbf{L} \times \mathbf{A} \rangle_{z,s}$ is shown in Figs. 19 and 20. For $n=2$ and 3, $\langle \mathbf{A} \rangle_z$ seems to be converging at some energy above 100 keV. The energy dependence of $\langle \mathbf{L} \times \mathbf{A} \rangle_{z,s}$ is similar for both $n=2$ and 3 for all energies. This unusual result may be useful in understanding the collision process.

While the available theories shown in Figs. 16–20 predict the energy dependence of the various quantities studied, they do not convey much physically intuitive information about the collision process. We hope that our results will provide an incentive for some new theoretical model based on the n scaling of simple collision parameters.

ACKNOWLEDGMENTS

The authors would like to thank Louis Dubé, Ashok Jain, Rajiv Shingal, and Henk Slim for making their calculations available prior to publication, and Eugen Merzbacher, Chii-Dong Lin, and Joachim Burgdörfer for fruitful discussions. The authors would like to acknowledge computational support from the Cornell National Supercomputer Facility, a resource of the Cornell Theory Center, which is funded in part by the National Science Foundation, New York State, the IBM Corporation, and members of the Center's Corporate Research Institute, and assistance from Hamamatsu Corporation and Hinds International Inc. in developing custom equipment for this experiment. This work was supported in part by NSF Grant No. PHY-90-16986.

[1] C. C. Havener, W. B. Westerveld, J. S. Risely, N. H. Tolk, and J. C. Tully, Phys. Rev. Lett. **48**, 926 (1982).
[2] C. C. Havener, Ph.D. thesis, North Carolina State University, 1983.
[3] C. C. Havener, N. Rouze, W. B. Westerveld, and J. S. Risely, Phys. Rev. Lett. **53**, 1049 (1984).
[4] C. C. Havener, N. Rouze, W. B. Westerveld, and J. S. Risley, Phys. Rev. A **33**, 276 (1986).
[5] C. D. Stone, M.S. thesis, North Carolina State University, 1986.
[6] J. R. Ashburn, R. A. Cline, C. D. Stone, P. J. M. van der Burgt, W. B. Westerveld, and J. S. Risely, Phys. Rev. A **40**, 4885 (1989).
[7] J. R. Ashburn, Ph.D. thesis, North Carolina State University, 1990.
[8] J. R. Ashburn, R. A. Cline, P. J. M. an der Burgt, W. B. Weserveld, and J. S. Risley, Phys. Rev. A **41**, 2407 (1990).
[9] R. A. Cline, W. B. Westerveld, and J. S. Risely, Phys. Rev. A **43**, 1611 (1991).
[10] K. Blum, *Density Matrix Theory and Applications* (Plenum, New York, 1981).
[11] H. J. Andrä, Phys. Rev. A **2**, 2200 (1970).
[12] I. A. Sellin, J. R. Mowat, R. S. Peterson, P. M. Griffin, R. Laubert, and H. H. Haselton, Phys. Rev. Lett. **31**, 1335 (1973).
[13] I. A. Sellin, L. Liljeby, S. Mannervik, and S. Hultberg, Phys. Rev. Lett. **42**, 570 (1979).
[14] G. Gabrielse, Phys. Rev. A **23**, 775 (1981).
[15] R. DeSerio, C. Gonzalez-Lepera, J. P. Gibbons, J. Burgdörfer, and I. A. Sellin, Phys. Rev. A **37**, 4111 (1988).
[16] T. G. Eck, Phys. Rev. Lett. **31**, 270 (1973).
[17] W. Harbich, R. Hippler, H. Kleinpoppen, and H. O. Lutz, Phys. Rev. A **39**, 3388 (1989).
[18] O. Plotzke, U. Wille, R. Hippler, and H. O. Lutz, Phys. Rev. Lett. **65**, 2982 (1990).
[19] D. Clarke and J. F. Grainger, *Polarized Light and Optical Measurement* (Pergamon, Oxford, 1971).
[20] M. Born and E. Wolf, *Principles of Optics* (Pergamon, Oxford, 1980).
[21] J. M. Bennett and H. E. Bennett, in *Handbook of Optics,* edited by W. G. Driscoll and W. Vaughan (McGraw-Hill, New York, 1978), pp. 164-207.
[22] W. B. Westerveld, North Carolina State University Technical Report, 1984 (unpublished).
[23] J. M. Ajello, S. K. Srivastava, and Y. L. Yung, Phys. Rev. A **25**, 2485 (1982).
[24] I. C. Malcolm, H. W. Dassen, and J. W. McConkey, J. Phys. B **12**, 1003 (1979).
[25] G. Gabrielse, Phys. Rev. A **22**, 138 (1980).
[26] R. Hippler, W. Harbich, M. Faust, H. O. Lutz, and L. J. Dubé, J. Phys. B **19**, 1507 (1986).
[27] P. R. Bevington, *Data Reduction and Error Analysis for the Physical Sciences* (McGraw-Hill, New York, 1969).
[28] R. A. Cline, Ph.D. thesis, North Carolina State University, 1991.
[29] M. C. Brower and F. M. Pipkin, Phys. Rev. A **39**, 3323 (1989).
[30] J. D. Jackson and H. Schiff, Phys. Rev. **89**, 359 (1953).
[31] C. Cohen-Tannoudji, B. Diu, and F. Laloë, *Quantum Mechanics* (Wiley-Interscience, New York, 1977).
[32] W. B. Westerveld, Comput. Phys. **3**, (5) 74 (1989).
[33] U. Fano and J. H. Macek, Rev. Mod. Phys. **45**, 553 (1973).
[34] G. Gabrielse and Y. B. Band, Phys. Rev. Lett. **39**, 697 (1977).
[35] J. Burgdörfer, Z. Phys. A **309**, 285 (1983).
[36] P. J. O. Teubner, W. E. Kauppila, W. L. Fite, and R. J. Girnius, Phys. Rev. A **2**, 1763 (1970).
[37] R. Hippler, O. Plotzke, W. Harbich, H. Madeheim, H. Kleinpoppen, and H. O. Lutz, Phys. Rev. A **43**, 2587 (1991).
[38] R. Hippler, O. Plotzke, W. Harbich, H. Madeheim, H. Kleinpoppen, and H. O. Lutz, Z. Phys. D **18**, 61 (1991).
[39] H. A. Slim, E. L. Heck, B. H. Bransden, and D. R. Flower, J. Phys. B **24**, 1991 (1991).
[40] R. Shingal and C. D. Lin, J. Phys. B **23**, L637 (1990).
[41] A. Jain, C. D. Lin, and W. Fritsch, Phys. Rev. A **36**, 2041 (1987).
[42] L. Dubé (private communication).
[43] E. W. Thomas, *Excitation in Heavy Particle Collisions* (Wiley, New York, 1972).
[44] E. P. Andreev, V. A. Ankudinov, and S. V. Bobashev, Zh. Eksp. Teor. Fiz. **50**, 565 (1966) [Sov. Phys. JETP **23**, 375 (1966)].
[45] D. Pretzer, B. Van Zyl, and R. Geballe, *Atomic Collision Processes,* edited by M. R. C. McDowell (North-Holland, Amsterdam, 1978), p. 618.
[46] D. Jaecks, B. Van Zyl, and R. Geballe, Phys. Rev. **137**, A340 (1965).
[47] R. L. Fitzwilson and E. W. Thomas, Phys. Rev. A **3**, 1305 (1971).
[48] D. H. Crandall and D. H. Jaecks, Phys. Rev. A **4**, 2271 (1971).
[49] V. Dose, Helv. Phys. Acta **39**, 683 (1966).
[50] L. Colli, F. Cristofori, G. E. Frigerio, and P. G. Sona, Phys. Lett. **3**, 62 (1962).
[51] G. Ryding, A. B. Wittkower, and H. B. Gilbody, Proc. Phys. Soc. London **89**, 547 (1966).
[52] R. H. Hughes, E. D. Stokes, S.-S. Choe, and T. J. King, Phys. Rev. A **4**, 1453 (1971).
[53] L. C. Biedenharn and J. D. Louck, *Angular Momentum in Quantum Physics* (Addison-Wesley, London, 1981), pp. 335–362.
[54] J. Burgdörfer, Phys. Rev. A **33**, 1578 (1986).
[55] C. D. Lin, R. Shingal, A. Jain, and W. Fritsch, Phys. Rev. A **39**, 4455 (1989).
[56] B. Van Zyl, M. W. Gealy, and H. Neumann, Phys. Rev. A **35**, 4551 (1987).
[57] J. Lenormand, J. Phys. (Paris) **37**, 699 (1976).
[58] J. S. Risely, F. J. de Heer, and C. B. Kerkdijk, J. Phys. B **11**, 1759 (1978).
[59] B. Van Zyl, M. W. Gelay, and H. Neumann, Phys. Rev. A **33**, 2333 (1986).
[60] C. F. Barnett, Oak Ridge National Laboratory Report No. ORNL-6086/V1, 1990 (unpublished).

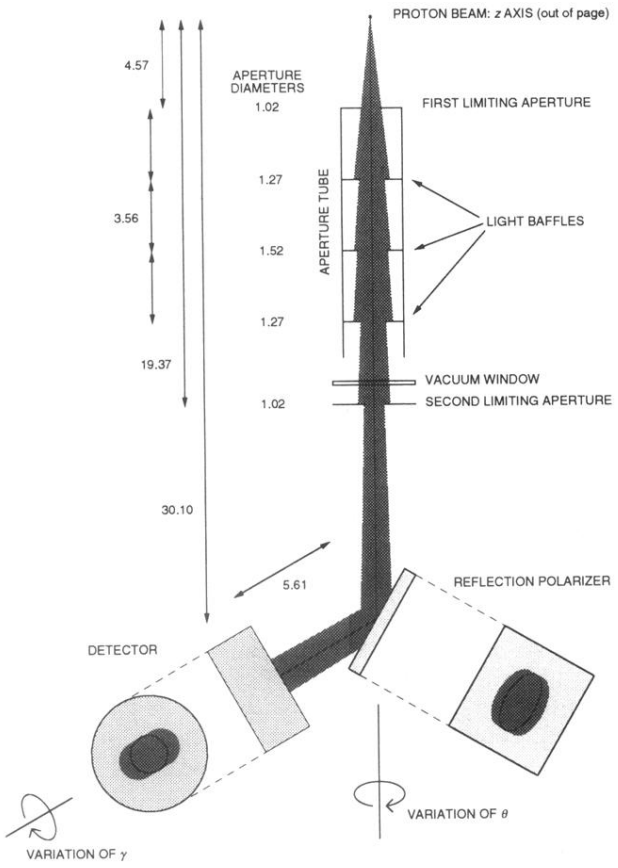

FIG. 2. Overview of the optical system. All dimensions are given in cm.

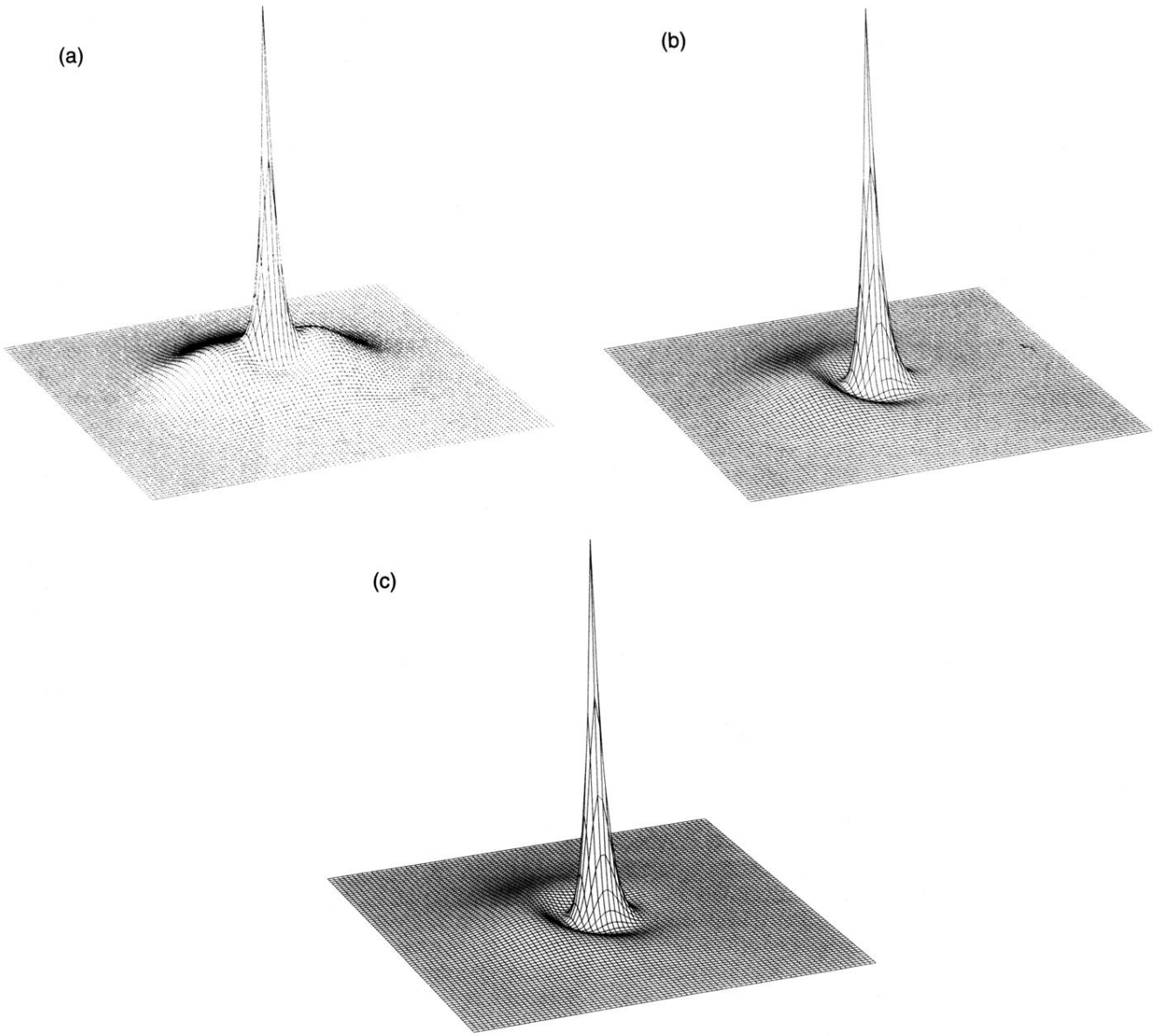

FIG. 6. Electronic charge-density distribution $D(\mathbf{r})$ for the H($n=2$) atoms. In this display the atoms are moving toward the right. The height indicates the probability to find the electron at that position in the xz plane. The scale is between ± 10 atomic units in each direction. (a) 20, (b) 40, and (c) 100 keV.